A leading order imaging series for prestack data acquired over a laterally invariant acoustic medium. Part II: Analysis for data missing low frequencies

Simon A. Shaw and Arthur B. Weglein
University of Houston

Abstract

The leading order imaging series images reflectors closer to their correct spatial location than a conventional depth imaging algorithm using the same reference velocity and without solving for the actual velocity model. The algorithm is a subseries of the inverse scattering series, a direct multidimensional inversion procedure, and is nonlinear in the measured wavefield. In this paper, we continue the progression of testing the effectiveness of the prestack leading order imaging series (Part I) for limited input data, specifically when the input data are missing low temporal frequency information, which is invariably the case in the seismic experiment.

It is demonstrated that, while it benefits from low frequency information, the leading order imaging series retains effectiveness even when zero and low frequency information are absent. Furthermore, its effectiveness is enhanced with offset data where the conjugate to depth $k_z = 2(\omega/c_0)\cos\theta$ replaces $k_z = 2(\omega/c_0)$ at normal incidence, allowing for a lower minimum k_z than is possible at normal incidence for the same temporal frequency bandwidth.

The relationship to low frequency information is analyzed by examining the imaging series' integral with respect to depth of the first term. It is shown that the fidelity of the construction of the first term in the low k_z band is important. However, the integration limits of the integral in the algorithm are not $-\infty$ to $+\infty$ and so the imaging series does not call for the zero frequency component of the data. We demonstrate using numerical reflectivity data examples, that even when missing zero and low temporal frequency information, the leading order imaging series improves the predicted depth of reflectors over conventional imaging with the reference velocity. While the imaging series is effective even when low frequencies are absent, greater effectiveness can be achieved when lower frequency information is present, which merits the study of existing and new spectral extrapolation techniques (Innanen et al., 2004), and is in perfect alignment with the current trend to acquisition systems that record lower frequency data.

These results are encouraging and justify the current progression of this and other inverse subseries algorithms to a multidimensional earth (Liu et al., 2004) and elastic wave equations (Zhang and Weglein, 2004).

1 Introduction

The development of inverse scattering series algorithms for seismic data processing begins with the isolation of a subseries that accomplishes a specific task, for example, free surface multiple removal, internal multiple attenuation or depth imaging (Weglein et al., 2003). Once a candidate subseries has been identified for the simplest earth and acquisition models, it is systematically analyzed under progressively more realistic conditions with the objective of developing it into an algorithm ready for field data.

The inverse scattering series, a multidimensional direct inversion procedure, is non-linear in the measured data. Other non-linear inverse methods (for example, Tarantola, 1987) have been found to fail in practice because field data are always band-limited, and missing low frequencies precludes a successful updating of the reference model towards the actual model. One important distinction between the inverse scattering series and iterative linear inversion is that, with the inverse series, the reference model is never updated. Every term in the inverse series is computed through an inversion of a dataset using only the original reference medium properties. Furthermore, the inverse subseries and task separation approach (Weglein et al., 2003), which inverts seismic data one step at a time, is in contrast to linear iterative inversion, which uses the total wavefield to directly invert for earth properties at once.

Despite significant differences between the inverse scattering subseries procedure and other non-linear inversion methods, it might be expected that at least one of the subseries algorithms would benefit from low frequency information. After all, they achieve seismic processing objectives without subsurface information by engaging the data more fully than algorithms that expect accurate *a priori* details about the medium. If the algorithms expect more from the data, then it is reasonable to think that at least one of them might benefit from a broad frequency spectrum. According to the convolutional model, a single frequency component from the source will experience the medium in a manner described by a linear differential operator before it is recorded at the receiver. The convolutional model applies to even the most complex absorptive elastic wave equations currently used to describe wave propagation. However, direct inversion of even the simplest single-parameter acoustic wave equation using the inverse scattering series requires communication between different frequencies.

The objective of this paper is to analyze the role of low frequency information in the leading order imaging series and, specifically, to answer the question of whether it retains any benefit when low frequency information is absent from the data. In preparation for the analysis, Shaw and Weglein (2004) derived this imaging series for prestack input data (Part I). This form of the algorithm expects input data that more closely represent the actual seismic experiment than a normal incidence algorithm because the source-receiver offset leads to a lower vertical wavenumber, k_z. The issue of missing low frequency in non-linear inversion is in fact one of missing low k_z, rather than missing low temporal frequency, ω.

3-D wave propagation in a constant density acoustic medium that varies only in 1-D (see

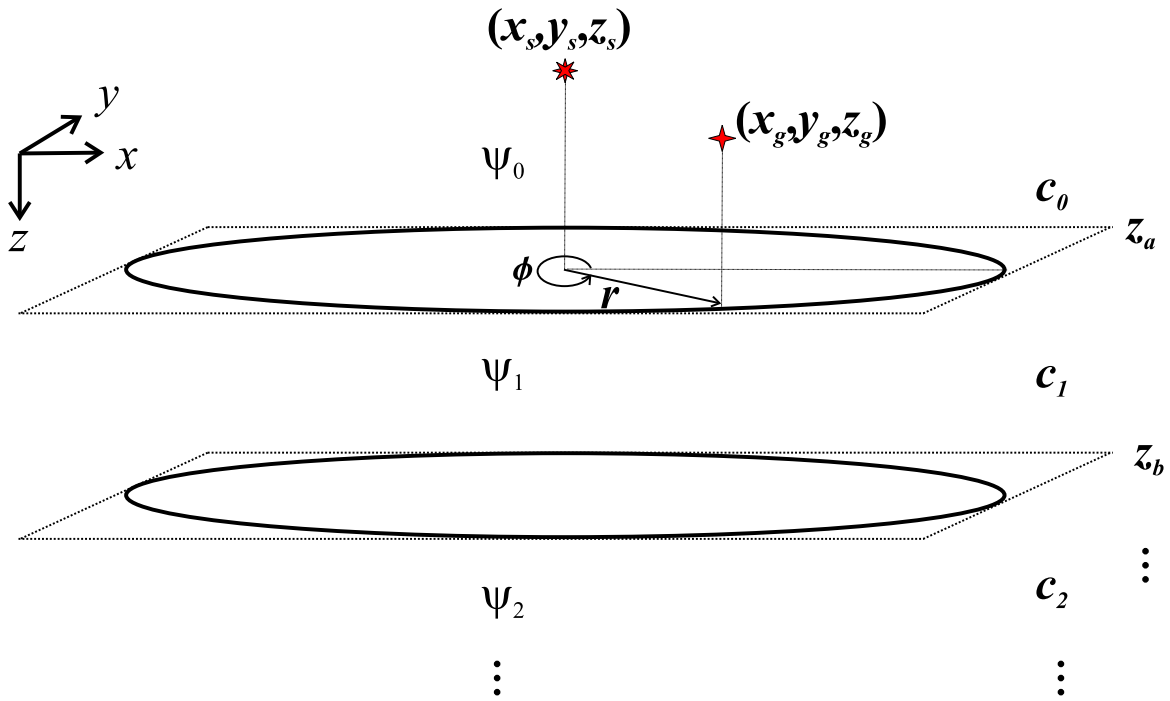

Figure 1*: A multi-layer 1-D constant density acoustic model.*

Fig. 1) is characterized by

$$\left(\nabla^2 + \frac{\omega^2}{c_0^2}\left(1-\alpha\left(z\right)\right)\right) P(\vec{x}\,|\vec{x}_{\,s};\omega) = -A(\omega)\delta(\vec{x}-\vec{x}_{\,s}) \tag{1}$$

where P is the pressure field, A is the source wavelet, ω is the angular temporal frequency, c_0 is the reference velocity and α is the velocity perturbation. In (1), the actual medium velocity, c, has been expressed in terms of a constant reference velocity, c_0, and the perturbation, α, where

$$\frac{1}{c^2\left(z\right)} = \frac{1}{c_0^2}\left(1-\alpha\left(z\right)\right). \tag{2}$$

The solution for α can be written as an infinite series

$$\alpha = \alpha_1 + \alpha_2 + \alpha_3 + \cdots \tag{3}$$

where α_1, the first term in the inverse series for α, is linearly related to the scattered field, $P_s = P - P_0$. P_0 is the pressure wavefield due to the same source, $A(\omega)$, in the reference medium, chosen to be a wholespace with velocity c_0. The second term, α_2, is quadratic in P_s, the third term, α_3, is cubic and so on.

The imaging series is responsible for positioning reflectors at their correct spatial location (Weglein et al., 2000, 2002). The objective of the imaging series, α^{IM}, a subseries of the

inverse series (3), is to solve directly for the *location* at which α changes. In other words, to solve for α^{IM} is to solve the problem of imaging in a medium whose velocity is not known before or after the imaging procedure. The leading order imaging series, α^{LOIM}, is the contribution to the imaging series that is leading order in the amplitudes of the scattered field (Shaw et al., 2003).

For the medium in which equation (1) describes wave propagation, and for a constant reference medium angle of incidence θ_0, the leading order imaging series can be written as an infinite sum of operations on the first term (Shaw and Weglein, 2004)

$$\alpha^{\mathrm{LOIM}}(z,\theta_0) = \sum_{n=0}^{\infty} \underbrace{\frac{(-1/2)^n}{n!\cos^{2n}\theta_0}}_{\text{Scalar}} \times \underbrace{\left(\int_0^z \alpha_1(z',\theta_0)dz'\right)^n}_{\substack{\text{Emphasizes low}\\ \text{frequency}}} \times \underbrace{\frac{d^n\alpha_1(z,\theta_0)}{dz^n}}_{\substack{\text{Emphasizes high}\\ \text{frequency}}} \tag{4}$$

where α_1 is computed through a scaled slant stack of the data, and in cylindrical coordinates is

$$\alpha_1(z,\theta_0) = -\,8\zeta_0\cos^2\theta_0 \int_0^{2\pi}\int_0^{\infty} D(r;\tau_0 - p_0 r\cos\phi)rdrd\phi. \tag{5}$$

The data are the scattered field with the source wavelet deconvolved ($D = P_s/A$), r is the source-receiver offset in the horizontal plane, ϕ is the azimuth, p_0 is the reference horizontal slowness, and ζ_0 is the reference vertical slowness.

In (4), we have labelled the parts of the algorithm according to their effect on the frequency spectrum of α^{LOIM}. The imaging series is a Taylor series for a box (i.e., the difference of two Heaviside functions) expanded about the depth of each mislocated interface. The coefficients of each term in the Taylor series are the product of the scalar with the integral of α_1. In the k_z domain, (4) is a power series for an exponential function. Recognizing this fact, then for a 1-D acoustic medium the leading order imaging series has a closed form solution:

$$\alpha^{\mathrm{LOIM}}(z,\theta_0) = \alpha_1\left(z - 1/(2\cos^2\theta_0)\int_0^z \alpha_1(z',\theta_0)dz',\theta_0\right). \tag{6}$$

This form will be used for the analysis in this paper. Studying the closed form focuses attention on the performance of the algorithm itself and not the numerical implementation of its series form. From (6), it is clear that the shift of each interface is proportional to the integral of α_1 above the reflector being imaged. This integral captures amplitude and residual moveout information in the overburden of each reflector and emphasizes $\tilde{\alpha}_1$ at low k_z values (because it is a division by k_z). The fidelity of α_1 and its integral will have a direct impact on the performance of the imaging series. Therefore, it is instructive to review the construction of $\tilde{\alpha}_1(k_z)$ from the data.

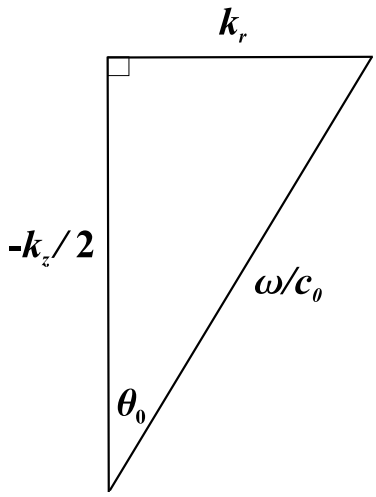

Figure 2*: The dispersion relationship between the vertical and horizontal wavenumbers and temporal frequency.*

2 Construction of the first term, α_1

In the wavenumber domain, the first term in the inverse series for the single parameter acoustic problem and a constant velocity reference medium is

$$\tilde{\alpha}_1(k_z) = 2\pi \frac{-k_z^2}{k_0^2} e^{-ik_z(z_g+z_s)/2} \int_0^\infty \tilde{D}(r;\omega) J_0(k_r r) r dr \tag{7}$$

where $k_0 = \omega/c_0$ and the vertical and horizontal wavenumbers, k_z and k_r, respectively, are related by (see Fig. 2)

$$k_z = -2\frac{\omega}{c_0}\sqrt{1 - \frac{k_r^2 c_0^2}{\omega^2}} = -2\omega\zeta_0. \tag{8}$$

$J_0(k_r r)$ is a zero order Bessel function of the first kind that arises due to the azimuthal symmetry and is

$$J_0(k_r r) = \frac{1}{2\pi}\int_0^{2\pi} e^{ik_r r cos\phi'} d\phi'. \tag{9}$$

The recorded data have spatial, temporal and wavenumber apertures. To keep the current discussion to the effect of missing low temporal frequency, it is assumed for the moment that the source-receiver offset aperture extends from $r = 0 \rightarrow \infty$.

By virtue of the source-receiver offset, the problem of determining $\tilde{\alpha}_1$ is over-determined since there are more free variables on the right-hand side of (7) than on the left. Hence, there is more than one way to compute $\tilde{\alpha}_1(k_z)$. For example, to compute $\tilde{\alpha}_1(k_z = 0)$, we

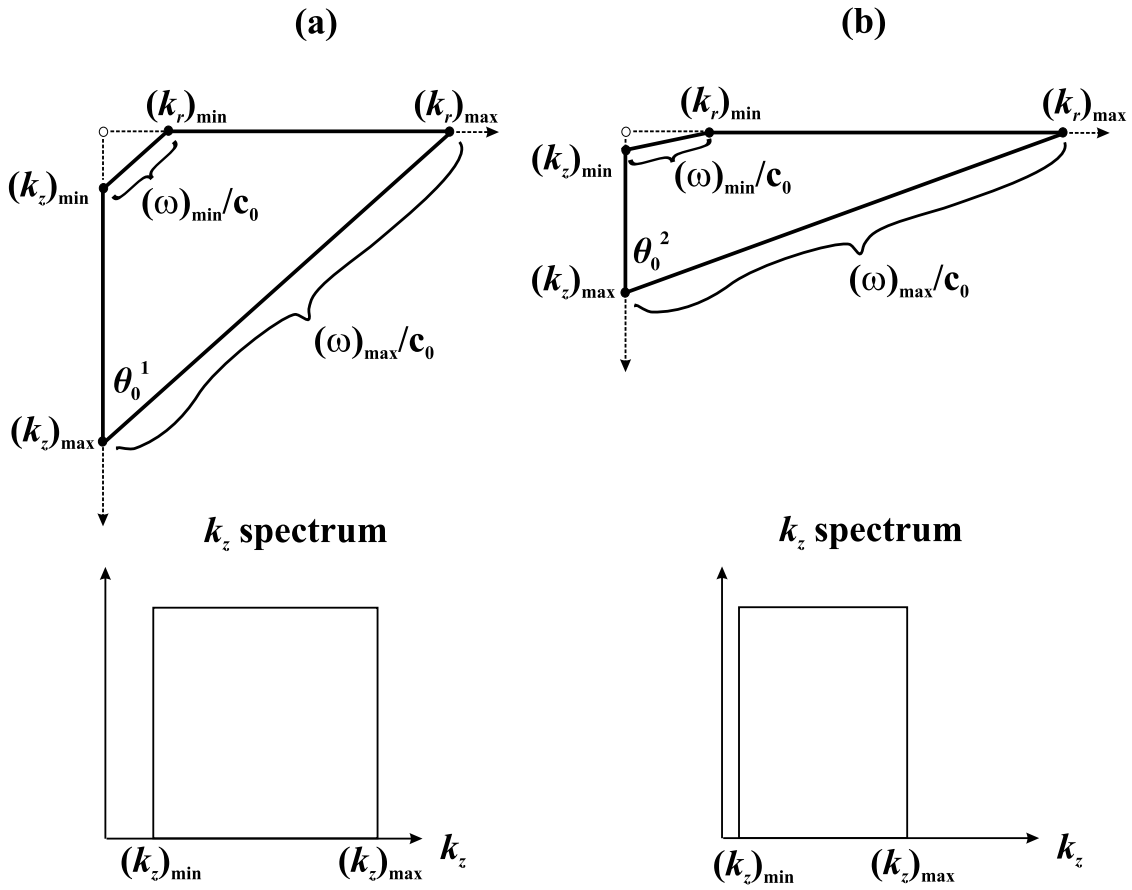

Figure 3*: The constraints imposed by bandlimited ω for two different angles of incidence, θ_0^1 and θ_0^2. Both $(k_z)_{min}$ and $(k_z)_{max}$ will be smaller for larger angles.*

can either set $\omega = 0$ or $k_r = \omega/c_0$. Since $k_z = -2k_0 \cos\theta_0$, then $k_z \to 0$ when $\theta_0 \to 90°$. Large angles of incidence can construct $\tilde{\alpha}_1$ at low k_z values. Inverse Fourier transforming both sides of (7) gives

$$\begin{aligned}\alpha_1(z) =& \frac{1}{2\pi}\int_{-\infty}^{\infty} \tilde{\alpha}_1(k_z) e^{ik_z z} dk_z \\ =& -\int_{-\infty}^{\infty} \frac{k_z^2}{k_0^2} e^{ik_z(z-(z_g+z_s)/2)} \int_0^{\infty} \tilde{D}(r;\omega) J_0(k_r r) r dr dk_z. \end{aligned} \tag{10}$$

Given the degree of freedom in the data, there is a choice regarding how to evaluate (10). Fixing the angle of incidence, θ_0, and integrating over angular frequency, ω, leads to different estimates of α_1 for each θ_0, denoted by $\alpha_1(z, \theta_0)$. This parameterization is illustrated in Fig. 3. Fixing θ_0 is the same as fixing horizontal and vertical slownesses, p_0 and ζ_0, respectively,

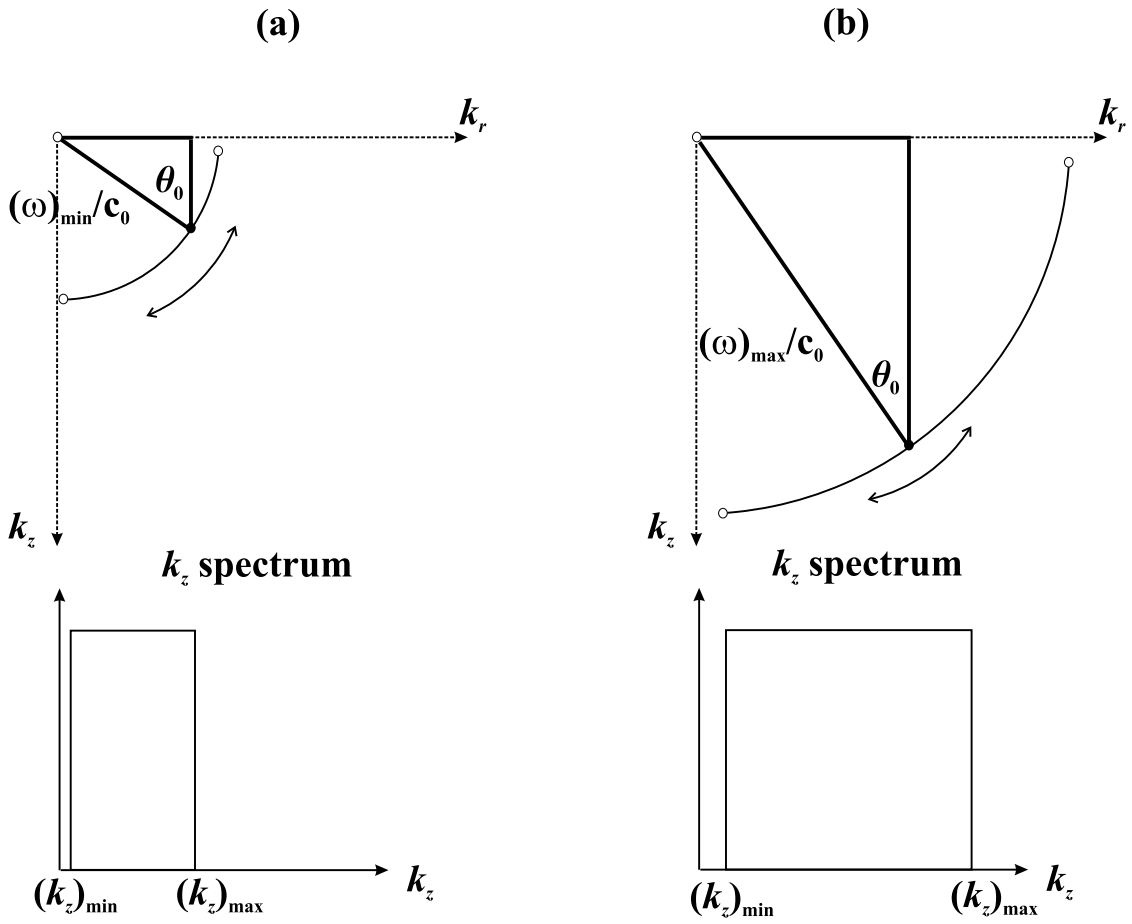

Figure 4*: The constraints imposed by bandlimited ω on the bandwidth of k_z when integrating over angle. This constant-frequency parametrization is an alternative to the one illustrated in Fig. 3 and is still under investigation.*

where

$$p_0 = \frac{\sin\theta_0}{c_0} \text{ and } \zeta_0 = \frac{\cos\theta_0}{c_0}.$$

An alternative approach to handling the degree of freedom in (10) is to keep ω fixed and integrate over angle or vertical slowness, ζ_0. This parameterization (illustrated in Fig. 4) will result in different estimates of $\alpha_1(z)$ for constant ω values and is the subject of ongoing research.

In this paper, we choose to hold θ_0 fixed which allows $(k_z/k_0)^2 = 4\cos^2\theta_0$ to come out of the outer integral in (10). Then, changing variables from k_z to ω (recalling $k_z = -2\omega\zeta_0$) gives

$$\alpha_1(z,\theta_0) = -\,8\zeta_0\cos^2\theta_0 \int_{-\infty}^{\infty} e^{-i\omega\zeta_0(2z-(z_g+z_s))} \int_0^{\infty} \tilde{D}(r;\omega) J_0(\omega p_0 r) r dr d\omega. \qquad (11)$$

Defining $\tau_0 = \zeta_0 (2z - (z_g + z_s))$ and performing the inverse temporal Fourier transform of the data $\tilde{D}(r;\omega)$, (11) becomes

$$\alpha_1(z,\theta_0) = -8\zeta_0 \cos^2\theta_0 \int_0^{2\pi}\int_0^{\infty} D(r;\tau_0 - p_0 r\cos\phi) r dr d\phi \tag{12}$$

$$= -8\zeta_0 \cos^2\theta_0 \int_{-\infty}^{\infty}\int_{-\infty}^{\infty} D(x,y;\tau_0 - x p_0) dx dy \tag{13}$$

which is recognizable as a scaled slant stack of the data (Treitel et al., 1982). As has been mentioned, it is assumed here that the data have infinite spatial aperture, so that the integrals in (12) and (13) can be evaluated accurately.

3 The effect of bandlimited data on the leading order imaging series at normal incidence

The data for a model that has two horizontal interfaces at depths z_a and z_b consist of two primary reflections. For a single frequency component,

$$\tilde{D}(r;\omega) = -\int_0^{\infty} \frac{R_{01} + R'_{12} e^{2i\omega\zeta_1(z_b - z_a)}}{i\omega\zeta_0} e^{i\omega\zeta_0(2z_a - z_s - z_g)} J_0(k_r r) k_r dk_r \tag{14}$$

where the reflection and transmission coefficients are functions of angle and are given by

$$R_{01} = \frac{\zeta_0 - \zeta_1}{\zeta_0 + \zeta_1}, R'_{12} = T_{01} R_{12} T_{10}, T_{01} = \frac{-2\zeta_1}{\zeta_0 + \zeta_1}, R_{12} = \frac{\zeta_1 - \zeta_2}{\zeta_1 + \zeta_2} \text{ and } T_{10} = \frac{2\zeta_0}{\zeta_0 + \zeta_1}. \tag{15}$$

The vertical slownesses are functions of the incident angles in each layer according to

$$\zeta_i = \frac{\cos\theta_i}{c_i} \ , \ \ i = 0, 1, 2, \ldots \tag{16}$$

Substituting the data (14) into the linear inverse equation (11), the first term in the series for $\alpha(z,\theta_0)$ is a sum over *all frequencies*

$$\alpha_1(z,\theta_0) = 8\cos^2\theta_0 \int_{-\infty}^{\infty} \left(\frac{R_{01} + R'_{12} e^{2i\omega\zeta_1(z_b - z_a)}}{i\omega} e^{2i\omega\zeta_0(z_a - z)} \right) d\omega. \tag{17}$$

Given all temporal frequencies, then (17) produces two Heaviside functions, one for each reflector:

$$\alpha_1(z,\theta_0) = 4\cos^2\theta_0 \left[R_{01}(\theta_0) H(z - z_a) + R'_{12}(\theta_0) H(z - z_{b'}) \right] \tag{18}$$

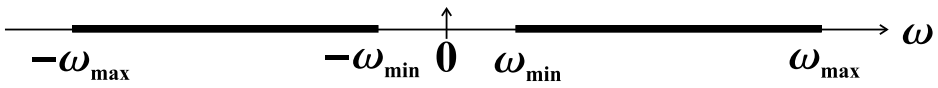

Figure 5*: In practice, ω will be bandlimited between ω_{min} and ω_{max}.*

where the shallower reflector is correctly located at z_a (since the velocity down to z_a was correct) but the deeper reflector is mislocated at depth

$$z_{b'} = z_a + (z_b - z_a)\frac{\zeta_1}{\zeta_0}. \tag{19}$$

In (18), it is emphasized that the amplitudes of each reflection event are functions of angle.

We proceed by first considering the special case of normal incidence, i.e., $\theta_0 = p_0 = 0$. The effect on $\alpha_1(z)$ when the ω spectrum is bandlimited (Fig. 5) is to produce bandlimited Heaviside functions. This is illustrated in Fig. 6 for a particular model (c_0=1500 m/sec, c_1=1650 m/sec, c_2=1510 m/sec, z_a=1000 m, $z_{b'}$=1075 m) and a range of different minimum frequencies ($f_{\min} = \omega_{\min}/(2\pi) = 0,\ 1,\ 2,\ 3$ Hz). Plotted beside each $\alpha_1(z, \theta_0 = 0)$ is its integral, which is an indication of how the leading order imaging series shift will be affected by missing low frequency information. As low frequency information is erased from the input data, the integral of α_1 deviates from its analytically computed values for infinite bandwidth. This error will impact the shift computed by the leading order imaging series as shown in Fig. 7. Even though the data contain no information below 1 Hz, the second interface still shifts towards the correct depth z_b because the integral of α_1 is a fair approximation to the exact value computed with infinite bandwidth. As a result of the error in the integral for $z \le z_a$, the reflector that was correctly imaged at z_a by α_1, is shifted slightly to a shallower depth.

The results in Fig. 7 can be significantly improved by recognizing that the area under the α_1 curve for $z < z_a$ is largely responsible for the error in the integral of α_1 at $z > z_a$ (see Fig. 6). It is known *a priori* that the perturbation $\alpha(z < z_a) = 0$ (and, by extension, $\alpha_1(z < z_a) = 0$) because the reference medium agrees with the actual medium at the measurement surface. It is not physically possible for the perturbation to be non-zero before the onset of the recorded reflectivity. This effect of missing low frequency can be straightforwardly rectified: rather than integrate from the measurement surface through an α_1 that is obviously in error, we choose to begin computing the integral at some small distance ϵ above the first reflector whose location is well-defined. We can further improve the integral of α_1, and impose a known condition, by fixing the value of the perturbation at $\alpha_1(z_a - \epsilon)$ to be zero and shifting all values of α_1 for $z > z_a - \epsilon$ by the value at $z_a - \epsilon$. Figure 8 illustrates the significant improvement in α_1 and its integral when making this simple correction. Implementing this causality-like condition in the leading order imaging series gives

$$\hat{\alpha}^{\mathrm{LOIM}}(z, \theta_0) = \alpha_1 \left(z - 1/(2\cos^2\theta_0) \int_{z_a - \epsilon}^{z} (\alpha_1(z', \theta_0) - \alpha_1(z_a - \epsilon, \theta_0))\, dz', \theta_0 \right). \tag{20}$$

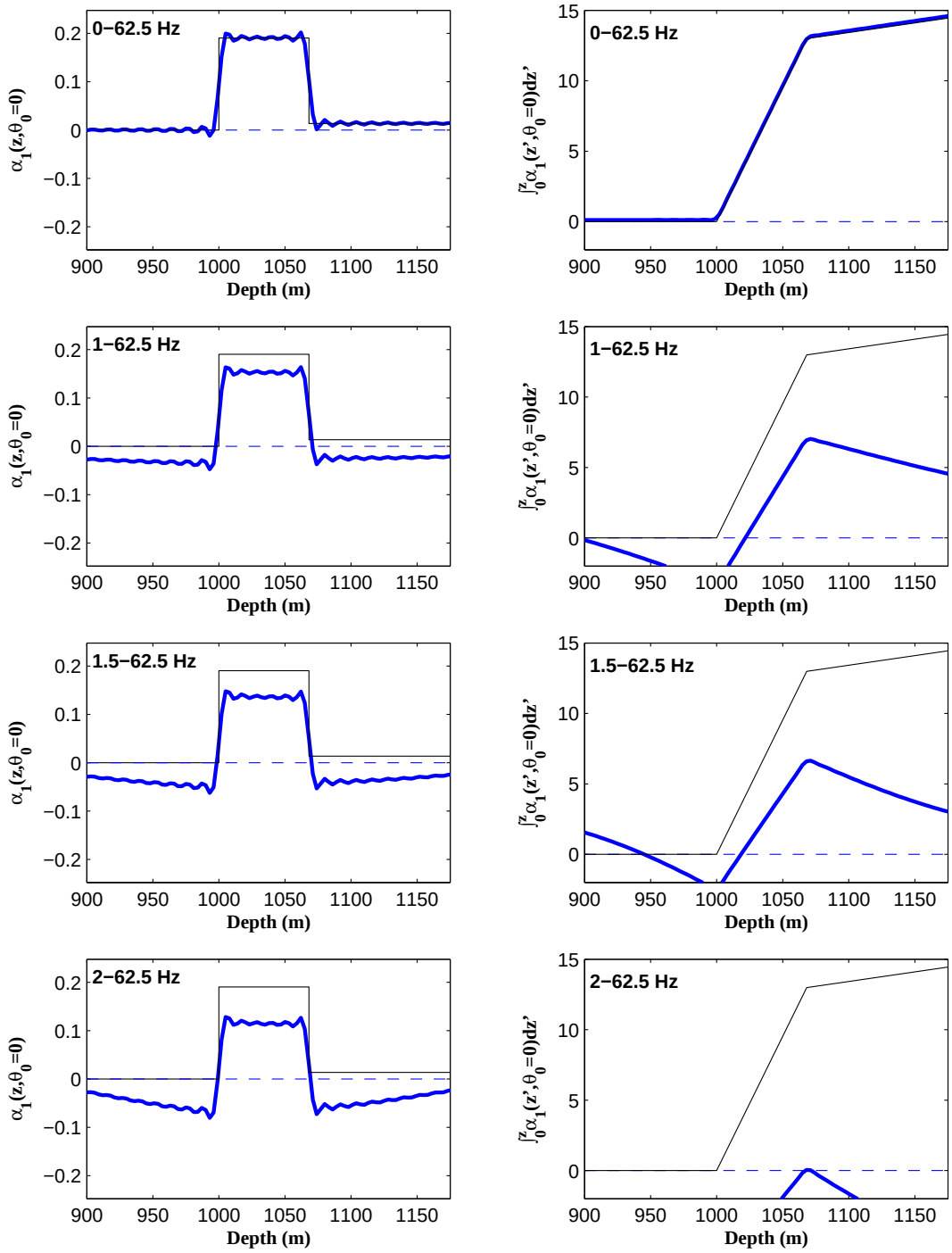

Figure 6: *The effect of missing low frequencies on $\alpha_1(z)$ (left) and its integral (right). The thin black lines are analytically computed values of α_1 and its integral for infinite bandwidth. The thick blue lines are the numerically computed values for bandlimited input data.*

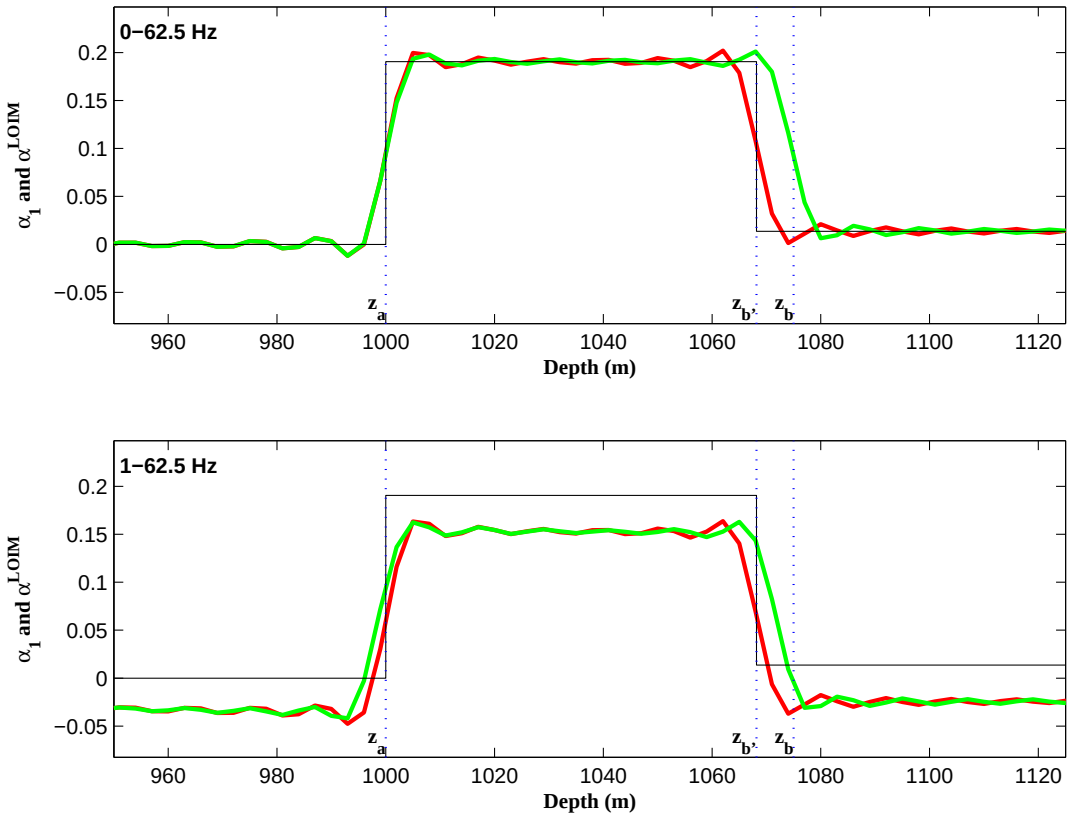

Figure 7: *The effect of missing low frequencies on $\alpha_1(z)$ (in red) and $\alpha^{LOIM}(z)$ (in green). Despite not having any information below 1 Hz, the second interface still shifts towards the correct depth z_b. There is a small error at the first interface which can be eradicated by changing the integration limits (Fig. 9).*

In all subsequent examples, we implement the leading order imaging series by imposing the condition that the perturbation must be zero before the onset of the scattered field (20). Then, for the same example as in Fig. 7, Fig. 9 shows the improvement in the result of the leading order imaging series when provided with this new integral of α_1.

Figures 10–12 show results of the leading order imaging series for a five-layer model (c_0=1500 m/sec, c_1=1600 m/sec, c_2=1550 m/sec, c_3=1625 m/sec, c_4=1510 m/sec, z_a=1000 m, z_b=1075 m, z_c=1125 m, z_d=1200 m) and a range of missing low frequencies up to 8 Hz. Figure 11 shows the same information as Fig. 10 except the derivatives with respect to z are displayed in order to more clearly identify the location of the reflectors. As demonstrated in Fig. 12, even after removing all information below 8 Hz (in this example), the leading order imaging series shows an improvement in the location of all reflectors.

Reducing the contrast between the actual and reference media is akin to having a reference velocity model that is a better estimate of the actual velocity. The effect will be apparent in the first term, α_1, because reducing the difference in the velocities means that the reflectors will be imaged closer to their true depths even before the non-linear terms are computed.

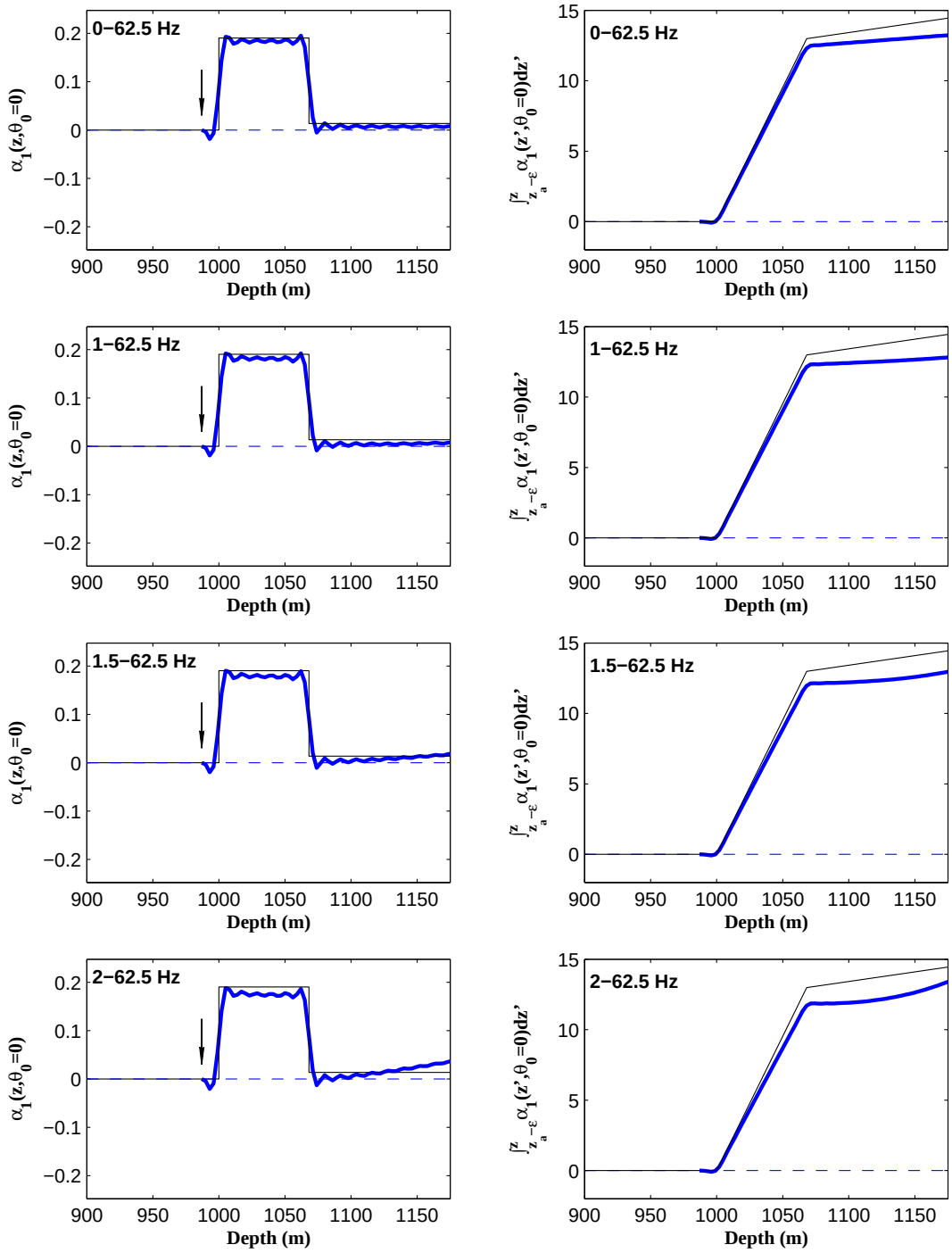

Figure 8: *The effect of missing low frequencies on $\alpha_1(z)$ and its integral when changing the integration limits from $\int_0^z$ to $\int_{z_a-\epsilon}^z$. Compared with Fig. 6, the results are significantly better when constraining the perturbation.*

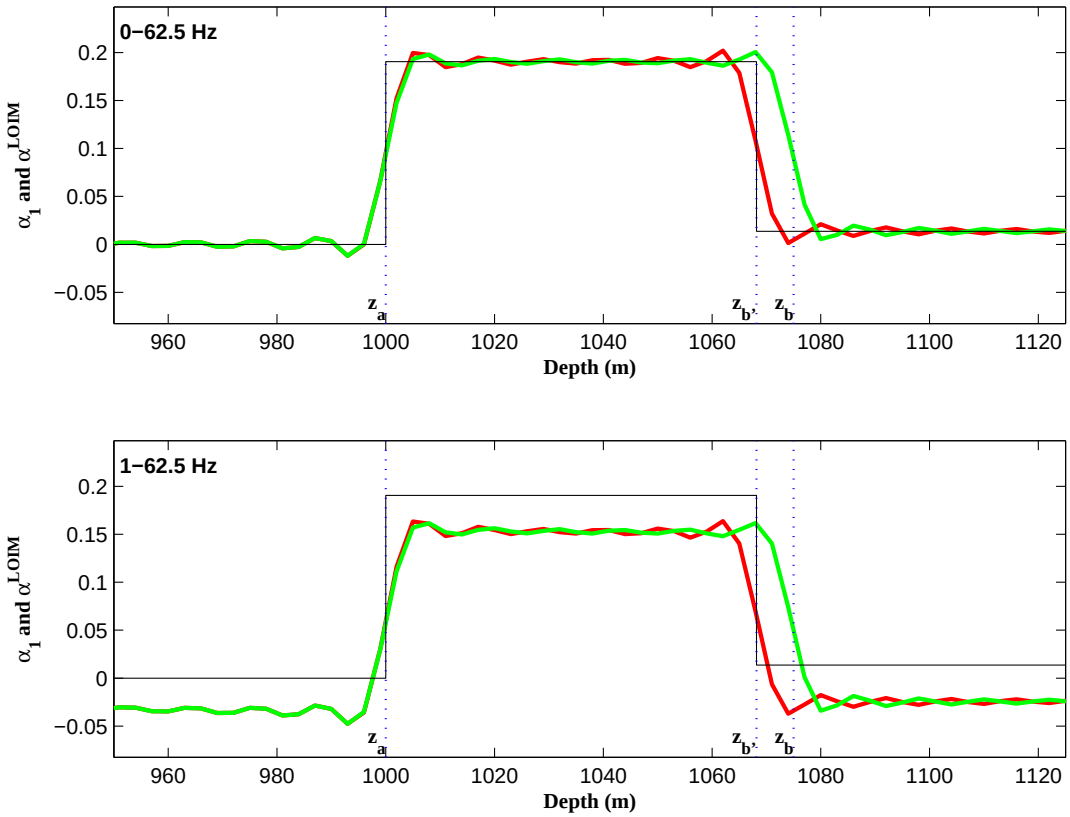

Figure 9*: By truncating the integral from* $\int_0^z$ *to* $\int_{z_a-\epsilon}^z$*, the major effect of missing low frequencies on* $\alpha^{LOIM}(z)$ *(in green) is greatly mitigated. In comparison with Fig. 7, the mislocated reflector has been accurately located by the imaging series.*

This is illustrated Fig. 13 where the velocity contrasts of the model in the top panel (labelled "Highest contrast") have been increased by 50% over those in the middle panel (labelled "Middle contrast") which are 50% greater than those in the bottom panel (labelled "Lowest contrast"). In each case, the lower frequency limit is 4 Hz and the *proportional* correction to the depths of the mislocated reflectors is approximately the same. Therefore, an increase in contrast would seem to not be more sensitive to missing low frequencies. The obvious benefit of lower contrasts, however, is that the closer the reference velocity is to the actual velocity, the better the leading order approximation is in the imaging series *and* the faster the series form will converge (Shaw et al., 2003). This observation regarding contrast and low frequency content is relevant to the next step in our analysis, which is to consider higher angles of incidence, where the effective contrast is greater.

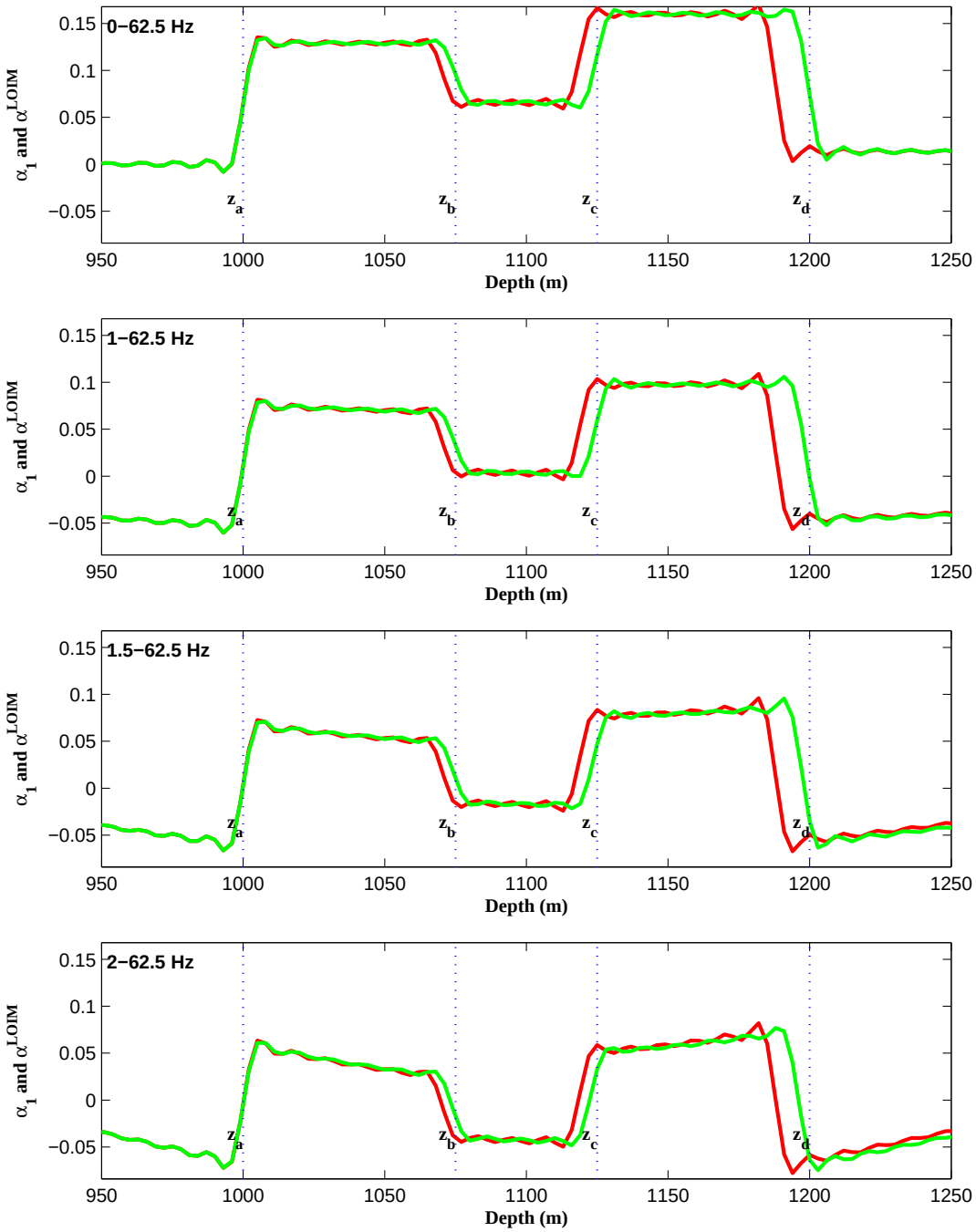

Figure 10: *A five-layer model comparing α_1 (in red) with α^{LOIM} (in green) for $\theta_0 = 0$ and different low frequency limits. The mislocated reflectors shift towards their true depths.*

4 The effect of bandlimited data at higher angles of incidence

As illustrated in Fig. 3, the degree of freedom afforded by the seismic experiment's source-receiver offset leads to a lower minimum vertical wavenumber, $(k_z)_{\min}$, in the construction

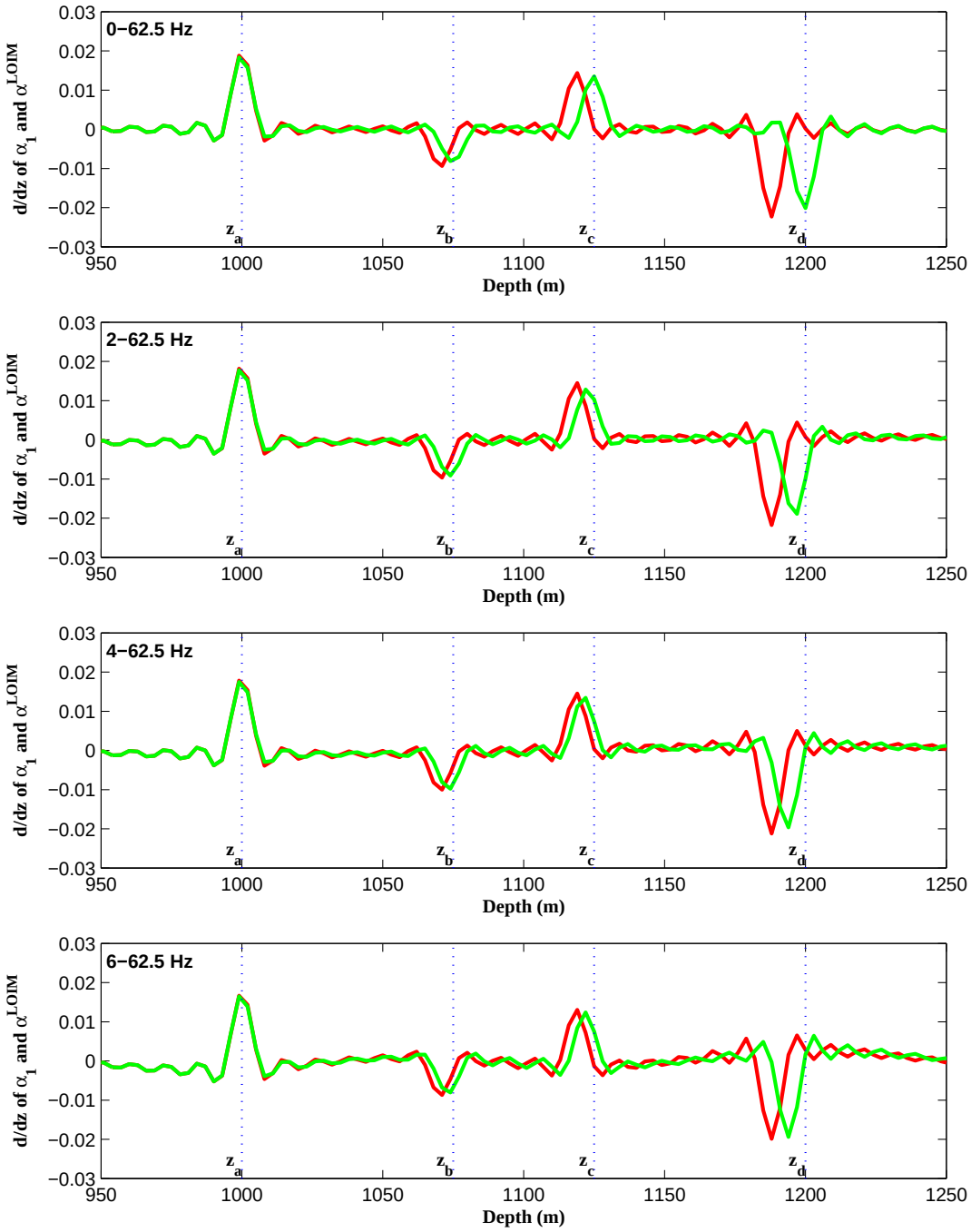

Figure 11: *A five-layer model comparing the derivatives with respect to z of α_1 (in red) and α^{LOIM} (in green) for $\theta_0 = 0$ and different low frequency limits. The mislocated reflectors shift towards their true depths.*

of $\tilde{\alpha}_1$ for higher angles of incidence through the relationship

$$(k_z)_{\min} = \frac{(\omega)_{\min}}{c_0} \cos\left[(\theta_0)_{\max}\right]. \tag{21}$$

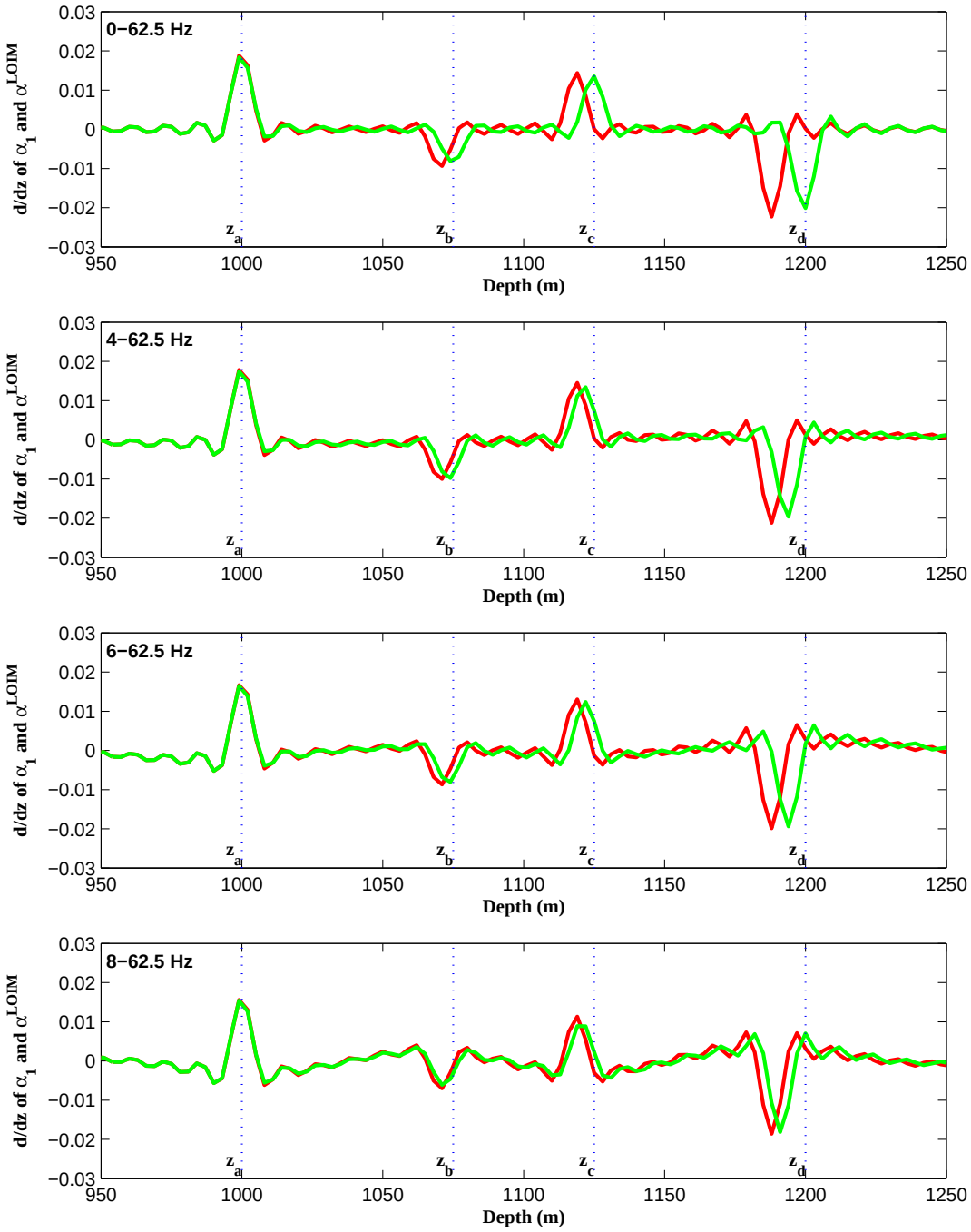

Figure 12: *A five-layer model comparing the derivatives with respect to z of α_1 (in red) and α^{LOIM} (in green) for $\theta_0 = 0$ and different low frequency limits (missing up to 8 Hz). Although there is a gradual degradation of the results when more low frequency is missing, in all cases the mislocated reflectors shift towards their true depths providing an improvement over linear imaging with the reference velocity.*

There are two factors that affect the amplitude of $\alpha_1(z, \theta_0)$ as a function of angle. The first is data-driven: the magnitude of the data's amplitudes (for these acoustic models) will tend to increase with angle. The second is algorithm-driven: the computation of α_1 involves a multiplication by $\cos^2\theta_0$. The net result, illustrated in Fig. 14 for the first interface (where there is no transmission loss in the recorded data), is that the amplitude of $\alpha_1(z, \theta_0)$ will tend to vary only gradually with angle. However, the leading order imaging series undoes the first term's algorithmic angle dependent scalar, $\cos^2\theta_0$, because higher angles of incidence will tend to have more residual moveout that needs to be corrected (Fig. 15). It is the larger magnitudes of the amplitudes with higher angles (Fig. 14) that set about correcting the greater error in depth (Fig. 15) through the imaging series algorithm (Shaw and Weglein, 2004).

The relevant question in the current analysis is how does the performance of the imaging series vary with angle when low temporal frequencies are missing? The results displayed in Fig. 13 would suggest that the higher "effective contrast" experienced at higher angles would be neither more nor less sensitive to missing low frequencies. However, in the leading order approximation to the imaging series that is currently being studied, higher contrasts will directly impact the accuracy of the predicted depths (Shaw et al., 2003). Specifically, the smaller the difference between the actual and reference media velocities, the more accurately the leading order imaging series will predict the precise locations of the reflectors.

Figure 16 demonstrates how higher angles of incidence fill in the low end of the k_z spectrum for 4−62.5 Hz bandlimited input data. At $\theta_0 = 0°$, the k_z spectrum derives no additional benefit at the low end in the sense that the $(k_z)_{\min}$ is equal to $(\omega)_{\min}/c_0$. However, at $\theta_0 = 45°$, $(k_z)_{\min}$ is reduced by the factor $\cos\theta_0$ and is equivalent to 2.8 Hz (as opposed to 4 Hz) at normal incidence. At higher angles, there is more residual moveout to be corrected for the nonlinear imaging terms.

Figure 17 shows results of the imaging series, for a fixed angle of incidence ($\theta_0 = 45°$), and a range of minimum temporal frequencies. It is encouraging to see that the difference in the predicted depths for $f_{\min} = 0.125$ Hz and $f_{\min} = 2$ Hz are extremely close and there are improvements over the first term for all cases where information below at least 6 Hz is missing.

In Fig. 18, the effect of missing low frequency on the prestack leading order imaging series is demonstrated on angle gathers over a range of precritical angles. While a gradual deterioration in effectiveness is evident as more low frequency information is removed, in all cases (at least up to $f_{\min} = 4$ Hz) for this example, the results of the imaging series are an improvement over conventional imaging with the reference velocity (i.e., the depths are more accurate than those predicted by the first term in the series).

It is interesting to consider whether the low k_z information at high angles can be transplanted to low angles of incidence to improve the performance of the leading order imaging series in the latter range. Figure 19 shows the effect of transplanting the low end of the k_z amplitude spectrum from $\alpha_1(z, \theta_0 = 50°)$ to the normal incidence trace, $\alpha_1(z, \theta_0 = 0°)$ over the range that it is missing and then computing the leading order imaging series. A small improvement

in the location of the deepest reflector is noticeable. This procedure resembles the alternative parameterization discussed earlier in which we can choose to keep omega constant and sum of angles to compute each term in the series, thereby collecting high angle information for each estimate of α^{LOIM}. This parameterization and procedure are currently under investigation.

5 Discussion

Analysis of the leading order imaging series algorithm for a 1-D acoustic earth that varies only in the z-direction, would suggest that low frequency information is important to its effectiveness because of its integral with respect to z. However, the limits of the integral are the reason why the algorithm can tolerate missing low frequency while still providing benefit. Thankfully, the algorithm does not call for

$$\int_{-\infty}^{\infty} \alpha_1(z')dz' \tag{22}$$

which is exactly the zero frequency component of the data. We have investigated procedures for improving the actual integral

$$\int_{0}^{z} \alpha_1(z')dz' \tag{23}$$

which collects the amplitude and moveout information in the overburden and acts to shift the mislocated reflectors towards their true locations in depth. One effective procedure that improves the accuracy of this integral derives from recognizing that the perturbation is before the onset of a reflector (say, at depth z_a). Redefining the integral to be

$$\int_{z_a-\epsilon}^{z} \alpha_1(z')dz' \tag{24}$$

significantly improves the results of the leading order imaging series when low frequencies are missing. To implement this causality-like condition, the first reflector could be automatically picked or else, if we had a good estimate of the medium velocity down to the top of salt (Fig. 20), we could build that into the reference medium and begin the imaging series at a depth below the subsurface.

The importance of low frequency information to the accuracy of the leading order imaging series motivates the study of methods for spectral extrapolation (Walker and Ulrych, 1983; Innanen et al., 2004). Larger angles of incidence and the concomitant lower k_z information is also expected to improve the accuracy of the depths predicted by the imaging series.

We note that trends in seismic data acquisition are towards the recording of lower frequencies. This is a welcome development as these and other new methods are developed that make full use of the recorded data's frequency spectrum.

6 Conclusion

We have demonstrated using reflectivity data in the precritical regime for a 1-D acoustic medium and 3-D wave propagation, that the leading order imaging series retains effectiveness, even when the input data are absent zero and low frequency information. This finding is critically important in the progression to a practical algorithm ready for application to field data. These conclusions merit the current generalization to a multidimensional earth (Liu et al., 2004) and more complex wave equations (Zhang and Weglein, 2004). The imaging of primaries at higher angles, especially in the post-critical regime is also of great interest (Nita and Weglein, 2004).

The imaging series is shown to benefit from having lower frequency information, in that reflectors will tend to move closer to their true depths than if the low frequency information is absent. Therefore, current trends towards acquiring lower frequency data, as well as existing and new methods for extrapolating this information are of keen interest.

Acknowledgements

ConocoPhillips (Hugh Rowlett and Rob Habiger) are thanked for their financial support (of S. A. Shaw) and for their encouragement of this research. Ken Matson and Gerhard Pfau at BP are thanked for releasing the reflectivity code and we are grateful to Dennis Corrigan for his support of that code. Bogdan Nita is thanked for his suggestions to improve this manuscript. We are grateful to the sponsors of M-OSRP for supporting this project.

References

Innanen, K. A., A. B. Weglein, and T. J. Ulrych (2004). Basic numerics in the non-linear inversion of primaries: simultaneous imaging and inversion II. *M-OSRP Annual Report 3*.

Liu, F., B. G. Nita, A. B. Weglein, and K. A. Innanen (2004). Inverse scattering series in the presence of lateral variations. *M-OSRP Annual Report 3*.

Nita, B. G. and A. B. Weglein (2004). Imaging with $\tau = 0$ versus $t = 0$: towards including headwaves into imaging and internal multiple theory. *M-OSRP Annual Report 3*.

Shaw, S. A. and A. B. Weglein (2004). A leading order imaging series for prestack data acquired over a laterally invariant acoustic medium. Part I: Derivation and preliminary analysis. *M-OSRP Annual Report 3*.

Shaw, S. A., A. B. Weglein, D. J. Foster, K. H. Matson, and R. G. Keys (2003). Isolation of a leading order depth imaging series and analysis of its convergence properties. *M-OSRP Annual Report 2*, 157–195.

Tarantola, A. (1987). *Inverse Problem Theory*. Elsevier Science B.V.

Treitel, S., P. R. Gutowski, and D. E. Wagner (1982). Plane-wave decomposition of seismograms. *Geophysics 47*(10), 1375–1401.

Walker, C. and T. J. Ulrych (1983). Autoregressive recovery of the acoustic impedance. *Geophysics 48*(10), 1338–1350.

Weglein, A. B., F. V. Araújo, P. M. Carvalho, R. H. Stolt, K. H. Matson, R. T. Coates, D. Corrigan, D. J. Foster, S. A. Shaw, and H. Zhang (2003). Inverse scattering series and seismic exploration. *Inverse Problems 19*, R27–R83.

Weglein, A. B., D. J. Foster, K. H. Matson, S. A. Shaw, P. M. Carvalho, and D. Corrigan (2002). Predicting the correct spatial location of reflectors without knowing or determining the precise medium and wave velocity: initial concept, algorithm and analytic and numerical example. *Journal of Seismic Exploration 10*, 367–382.

Weglein, A. B., K. H. Matson, D. J. Foster, P. M. Carvalho, D. Corrigan, and S. A. Shaw (2000). Imaging and inversion at depth without a velocity model: Theory, concepts and initial evaluation. In *70th Annual Internat. Mtg., Soc. Expl. Geophys., Expanded Abstracts*, pp. 1016–1019. Soc. Expl. Geophys.

Zhang, H. and A. B. Weglein (2004). Target identification using the inverse scattering series: data requirements for the direct inversion of large-contrast, inhomogeneous elastic media. *M-OSRP Annual Report 3*.

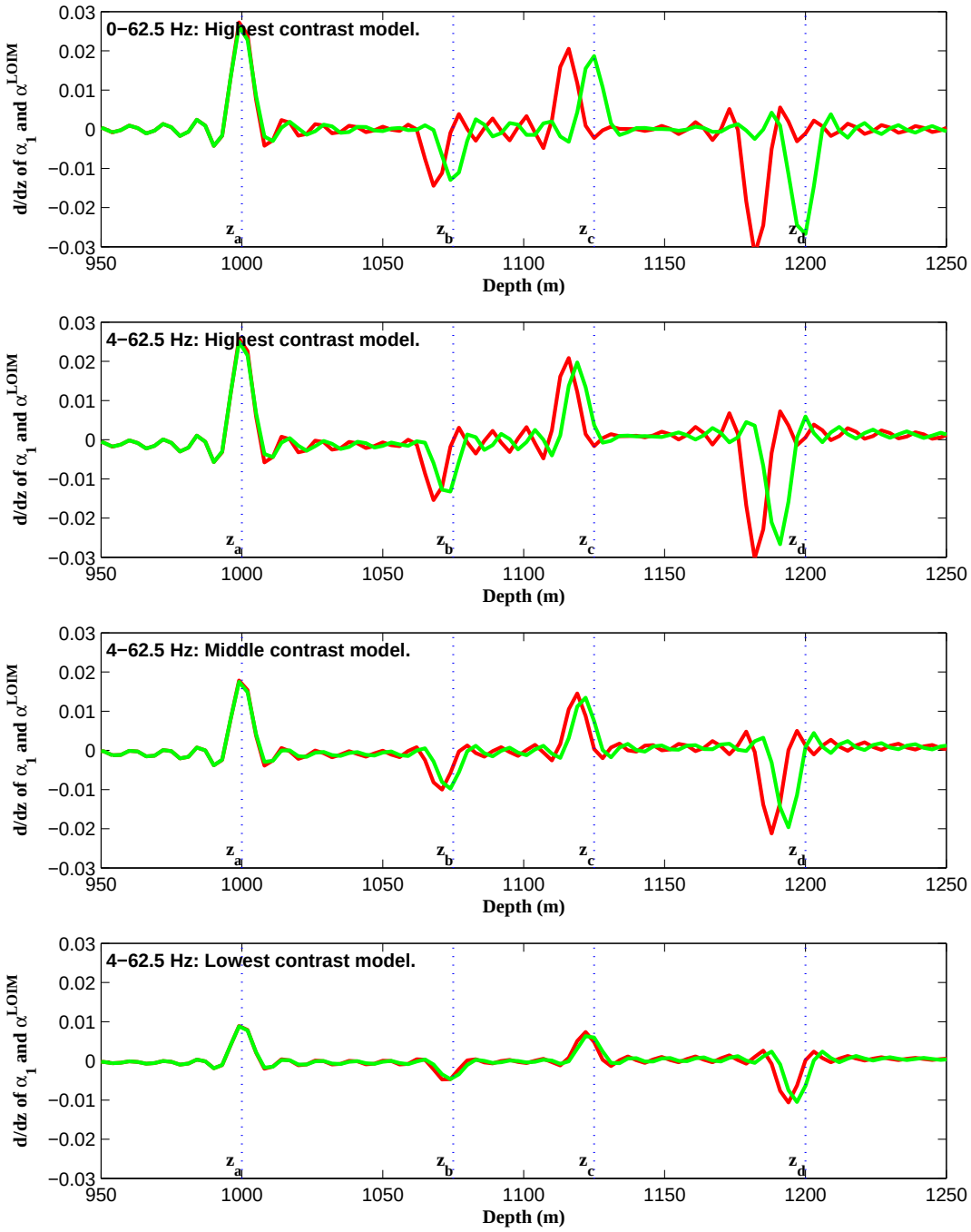

Figure 13: *The effect of contrast between the actual and reference medium on the leading order imaging series for data missing low temporal frequency. A comparison of the derivatives with respect to z of α_1 (in red) and α^{LOIM} (in green) for $\theta_0 = 0$ and three different five-layer models. At top is the result for data that have all low frequencies, including zero frequency. In the other cases the low frequency limit is 4 Hz. The "middle contrast" model is the same as in Figs. 10-12 and the other two deviate from it by $\pm 50\%$ in their interval velocities.*

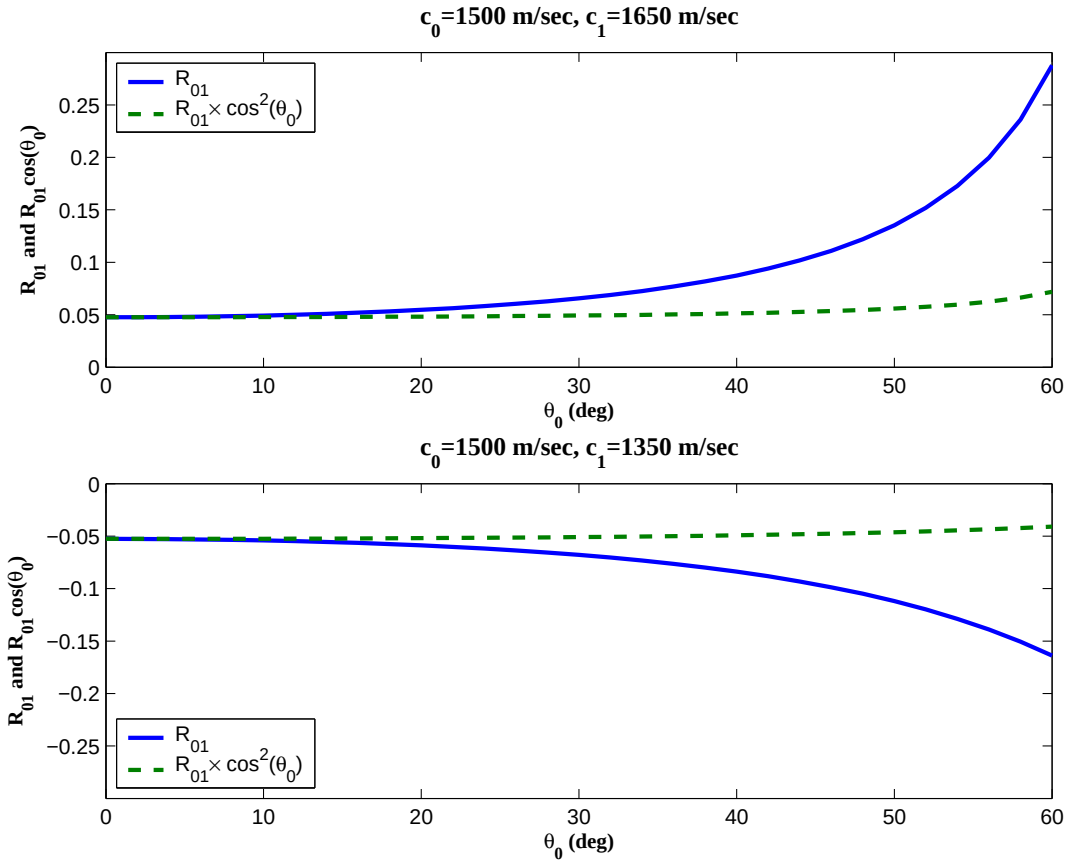

Figure 14*: The variation of reflection coefficient at the first interface ($z = z_a$) as a function of angle for two different models. The first term in the inverse series, α_1, is proportional to $\cos^2\theta_0$ times the data's amplitudes. The net result is that the amplitudes in α_1 will tend to vary more gradually with angle than the amplitudes in the data.*

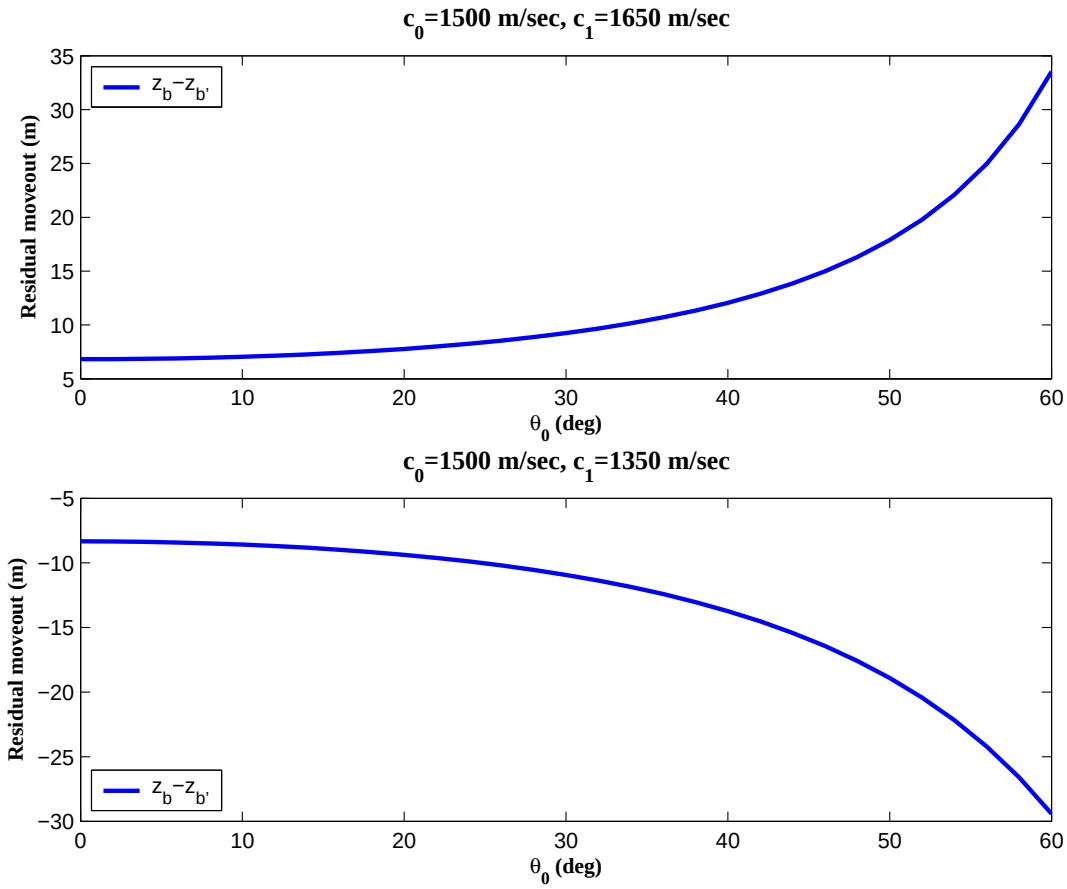

Figure 15*: The residual moveout for two different models corresponding to Fig. 14. z_b is the actual depth of a reflector and $z_{b'}$ is its depth predicted by the first term in the imaging series (i.e., through a conventional migration).*

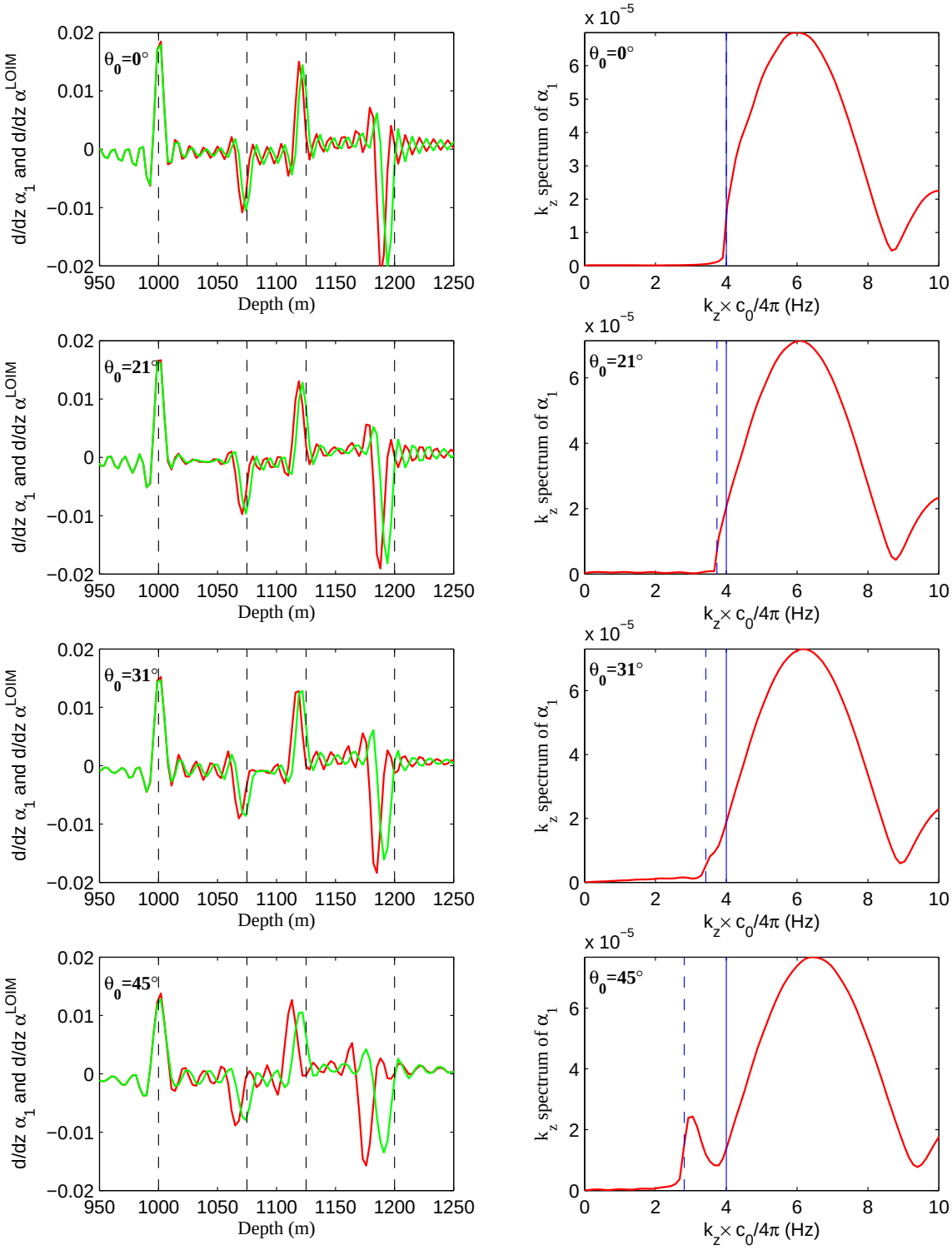

Figure 16: *Filling in the low end of the k_z spectrum according to (21) for 4−62.5 Hz bandlimited input data. A comparison, for four different angles of incidence, of α_1, (in red) and α^{LOIM} (in green) and the k_z spectrum of α_1 in each instance (on right).*

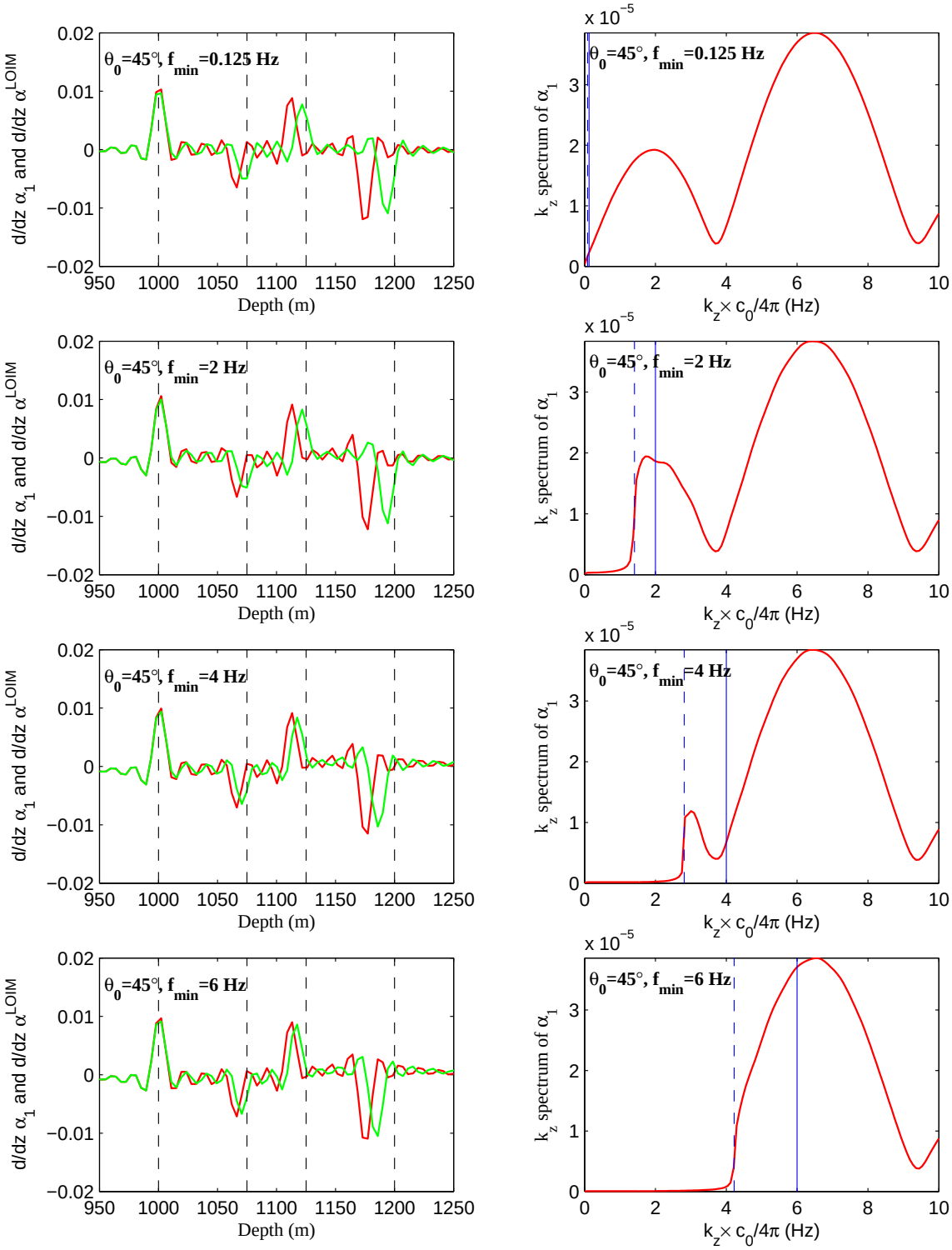

Figure 17: *A comparison of α_1 (in red) and α^{LOIM} (in green) and the k_z spectrum of α_1 (on right) for four different low frequency limits. The filling in of the low end of the k_z spectrum according to (21) is apparent. The difference in the depths predicted by the imaging series when having down to 0.125 Hz (top) and only having down to 2 Hz (second from top) is hardly noticeable.*

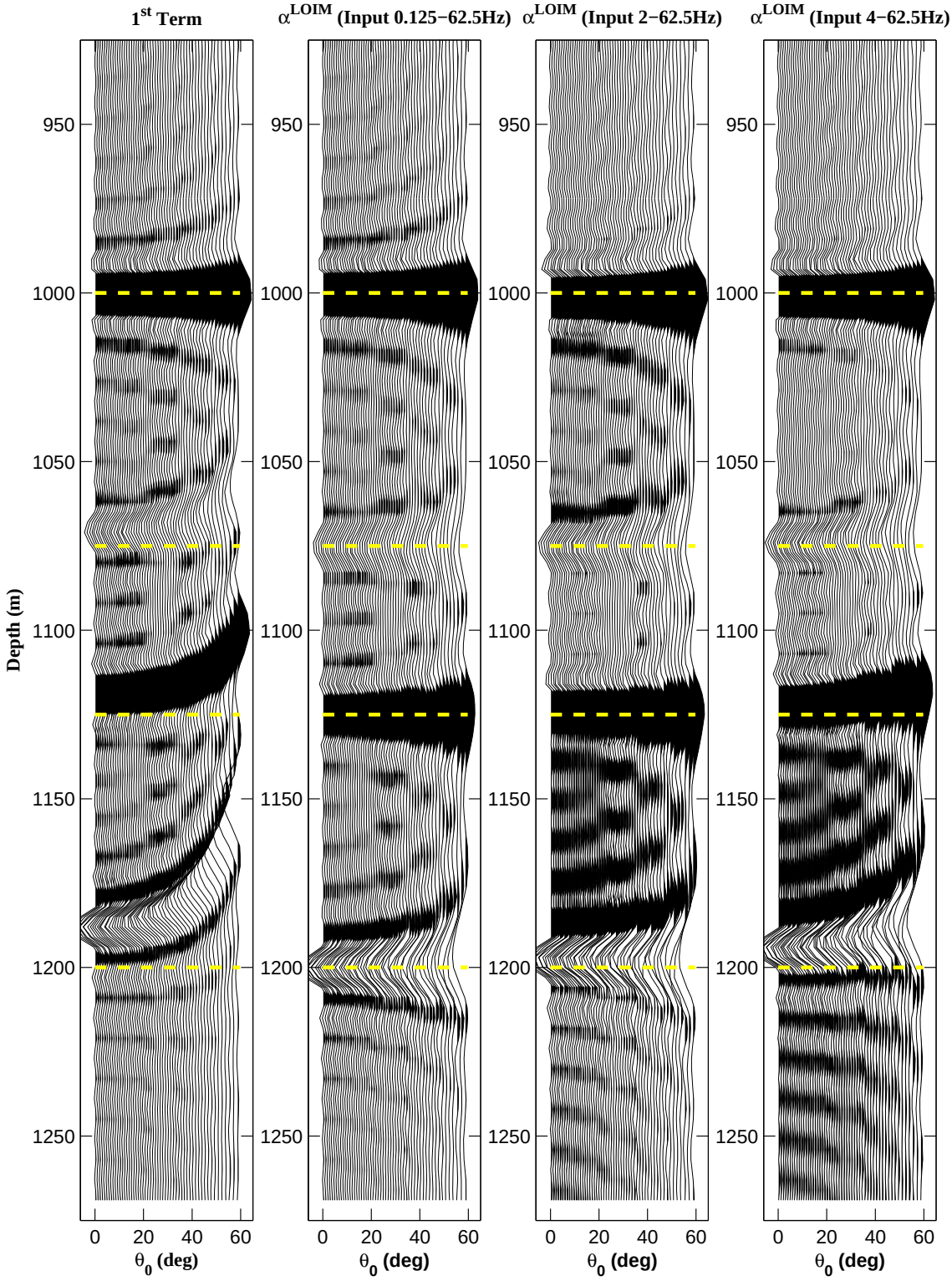

Figure 18*: Prestack leading order imaging series for a range of different low frequency limits. The left panel is the first term in the series, which exhibits typical residual moveout. The other three panels are the closed form result of the leading order imaging series. As more low frequency information is removed, the leading order imaging series results deteriorate but, in all cases, the results are an improvement over the first term.*

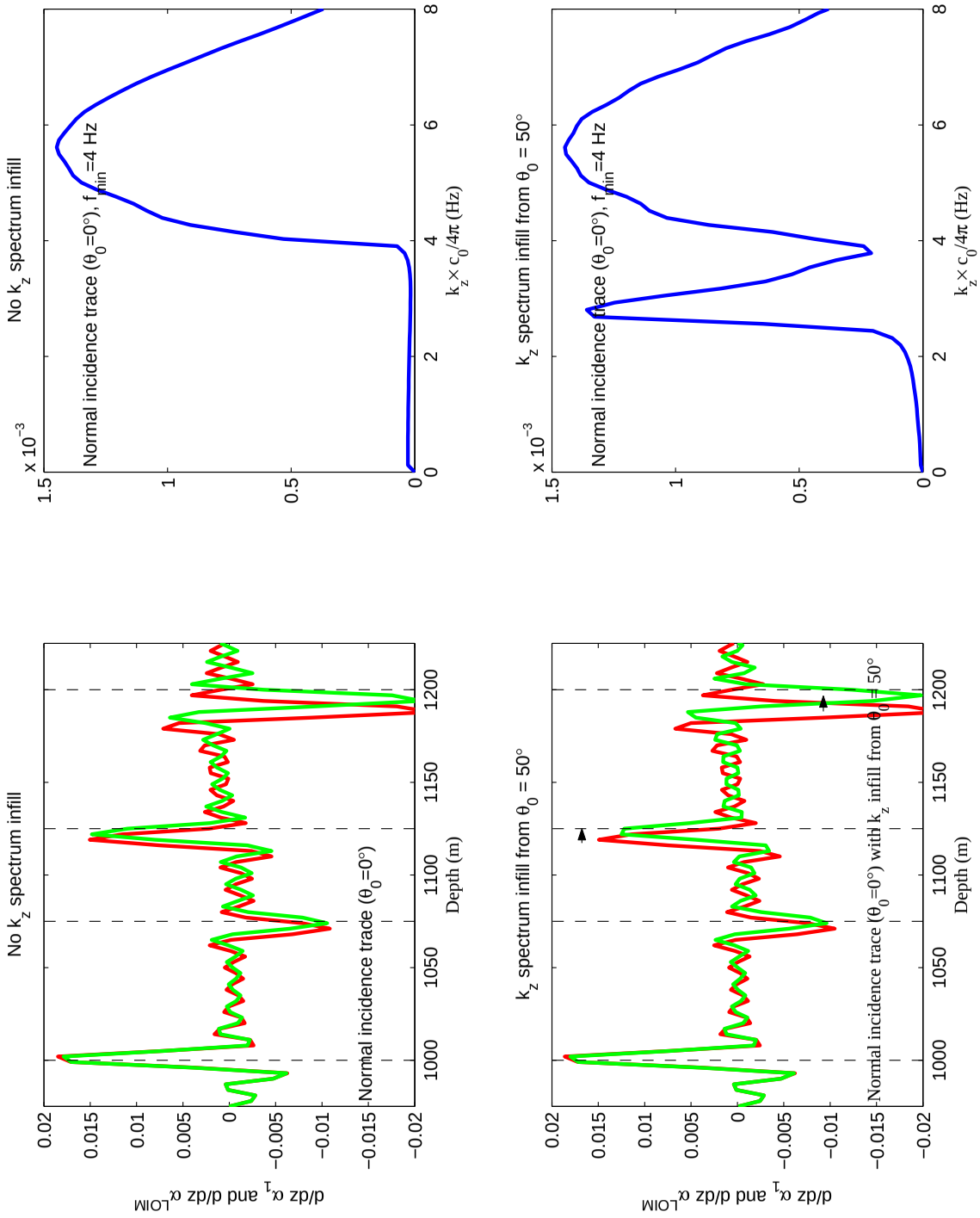

Figure 19*: The effect of transplanting low k_z information from the trace at* 50° *to the normal incidence trace for 4−62.5 Hz bandlimited input data. A small improvement is noticeable at the deepest reflector.*

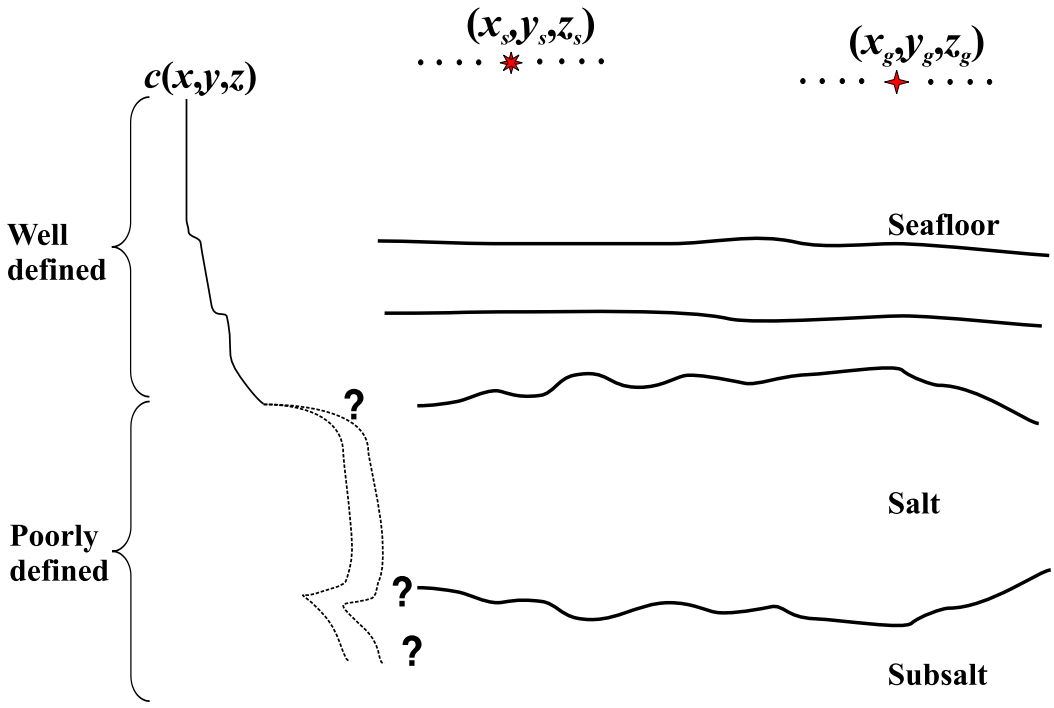

Figure 20*: The problem of subsalt imaging is sometimes described as a combination of complex, rugose top and bottom of salt and weak reflectivity below salt. The velocity down to the top of salt can often be adequately estimated using conventional velocity anlysis techniques.*